Multipath Scattering in Ultrawide-Band Radar Sea Spikes

Mark A. Sletten, *Member, IEEE*

***Abstract*—This paper presents sea-scatter data collected with an ultrawide-band (UWB) polarimetric radar system that indicates that multipath scattering plays an important role in the generation of sea spikes. The radar system used in this study produces short pulses with a bandwidth of approximately 3 GHz centered at 9 GHz for a range resolution of approximately 4 cm. Pulse-to-pulse switching allows collection of the microwave echoes produced by all four combinations of linear transmit and receive polarizations [vertical-transmit vertical-receive (VV), horizontal-transmit horizontal-receive (HH), horizontal-transmit vertical receive (HV), and vertical-transmit horizontal-receive (VH)] each of which is collected by a sampling oscilloscope utilizing equivalent time sampling. In June 1996, upwind sea scatter data at grazing angles of 10°, 20°, and 30° were collected while the system was deployed on a research pier on the Outer Banks of North Carolina. An analysis of the strongest echoes (sea spikes) from this data set is presented and discussed in this paper. First, the cumulative distribution functions are presented. Second, an increase of approximately 5 dB is shown to occur in the polarization ratio (HH/VV) of the strongest echoes as the grazing angle decreases from 30° to 10°. Third, differences in the spatial and spectral characteristics of the VV and HH spikes are described. Through comparisons with laboratory results and a simple scattering model, these observations are explained by the presence of a multibounce scattering mechanism. The use of the model to extract wave height from the sea-spike frequency response is also explored.**

***Index Terms*—Sea-surface electromagnetic scattering.**

I. Introduction

RADAR sea scatter in the low-grazing angle regime has been an area of active research for several decades due to its importance to shipboard radar design and remote sensing. But despite many years of research, existing models fail to describe some of its important features. "Sea spike" is the term used to describe one such characteristic of high-resolution backscatter from the sea—the high-amplitude clutter signals that often punctuate the otherwise low-level backscatter for horizontal (HH) polarization. Such events, in which the ratio of the horizontal to vertical signal levels can greatly exceed 0 dB, are not explained by the standard Bragg or two-scale scattering models. Most analyzes now indicate that vertically (VV) polarized backscatter from the sea can be adequately described by existing two-scale models, but that HH polarization needs to be characterized by a two-scale model plus an independent process that predicts the spikes and raises the overall level of the backscatter. For example, McLaughlin *et al.* [1] have measured fully polarimetric backscatter from the sea at 3° grazing and found that polarimetric signatures of sea spikes indicate the presence of two independent processes, whereas signatures in the absence of spikes infer only one. Hansen and Cavaleri [2] and Olin [3] have found that the distribution functions of VV backscatter can be fitted with a single Weibull distribution, while HH polarization requires two independent distributions, indicating that two processes are present. Trizna [4], Smith *et al.* [5], Lee *et al.* [6], and Rozenberg *et al.* [7] also find that a combination is necessary to explain measured Doppler spectra—one to explain the lower amplitude statistics and one to explain the higher amplitude, higher Doppler events.

While it is now generally accepted that additional mechanisms are at work, the underlying physics are not yet fully understood. Laboratory measurements by Sletten and Wu [8], Ebuchi *et al.* [9], and Trizna *et al.* [10] indicate that the highest amplitude echoes are associated with the fast moving crests of sharp-crested or breaking waves. Lee [6] and Eckert [11] draw similar conclusions from field data. Jessup *et al.* [12] have quantified the contribution of sea spikes to the overall radar cross section, but their results may not apply outside of the mid-incidence regime (45°) where the data was collected. Sletten and Wu [8] and West and Sletten [13] have measured and simulated ultrawide-band (UWB) radar backscatter from spilling breakers in a wavetank and have determined that the scattering mechanism is dominated by multipath. Trizna [14] has recently modeled the effect of multipath and Brewster angle damping on low-grazing-angle sea scatter and found that this combination can account for differences observed in the amplitude characteristics of VV and HH polarized backscatter. Hanson and Zavorotny [15] have also developed a model in which multipath and Brewster angle effects play a central role. Wedge [16] and plume [17] models have also been investigated.

In this paper, a polarimetric, UWB radar system is used to investigate the scattering mechanisms responsible for sea spikes. Such a system offers several advantages over conventional radars when used for this purpose. First, with the extremely high-range resolution afforded by several gigahertz of bandwidth, individual scatterers on the sea surface can be resolved and studied. Second, the wide percentage bandwidth provides information on the *frequency response* of the scatterer that can be used to infer the scattering mechanism. Third, the polarimetric capability provides an additional dimension in which the scattering problem can be investigated and in which potential models can be tested.

Manuscript received May 10, 1997; revised October 3, 1997.

The author is with the Naval Research Laboratory, Code 7255, Washington, DC 20375 USA.

Publisher Item Identifier S 0018-926X(98)01032-1.

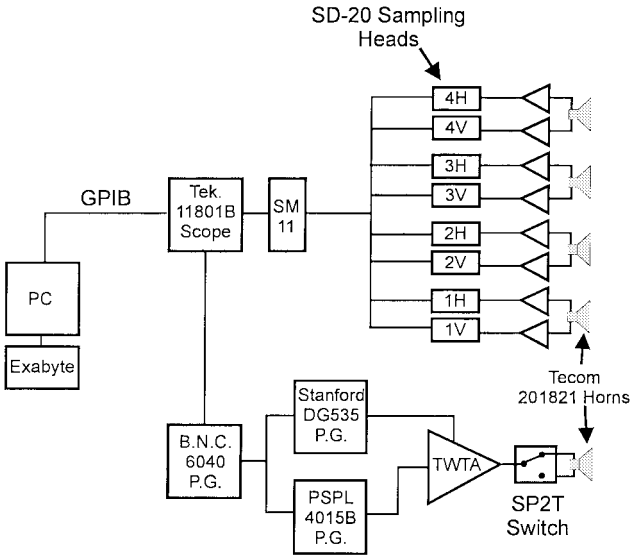

Fig. 1. Block diagram of the UWB radar system.

In the following section, the UWB system used in this research is described. In Section III, the experimental setup and the conditions under which the data were collected are reported. This is followed in Section IV by the cumulative distribution functions of the data, an analysis of the polarization ratio of the strongest sea spikes, and a representative sample of the sea-spike waveforms and corresponding radio frequency (RF) spectra. In Section V, these results are compared to previous laboratory studies and to a simple scattering model, both of which indicate that multipath plays a significant role in the scattering mechanism. The paper concludes in Section VI with a summary.

II. UWB Radar System Description

Fig. 1 contains a diagram of the radar system used in this research. The system is comprised of commercial off-the-shelf components. A multichannel sampling oscilloscope serves as a data acquisition system and several pulse generators and a traveling wave tube amplifier (TWTA) form the transmitter section. The system is similar in principle to the laboratory system developed by Sletten and Trizna [18], but has considerably more RF power and channel capacity.

The transmitter is formed by three pulse generators and a TWTA. A Berkeley Nucleonics Corporation (BNC) Model 6040 pulse generator with a 150-ps rise time is used as a master trigger source. The BNC pulse is used to trigger a Picosecond Pulse Labs (PSPL) Model 4015B pulse generator to produce a 15-ps rise time, 9-V step. This fast step excites a Logimetrics Model A750/XU-704A TWTA, generating a pulse with a 3-dB bandwidth of 3 GHz, a center frequency of 9 GHz, and a peak power of approximately 1 kW. This pulse and its spectrum are shown in Fig. 2(a) and (b), respectively. As shown, the pulse consists of several 9–10 GHz oscillations for a 3-dB pulse width of approximately 0.3 ns and a corresponding range resolution of 4 cm. This technique for generating short pulses has been used previously at NRL [19], [20]. A high-power UWB switch is used to direct the pulse between the horizontal and vertical ports of the transmit antenna—a

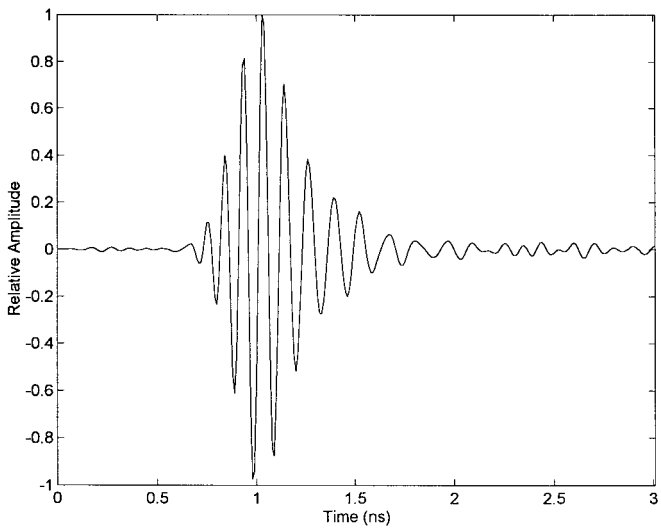

(a)

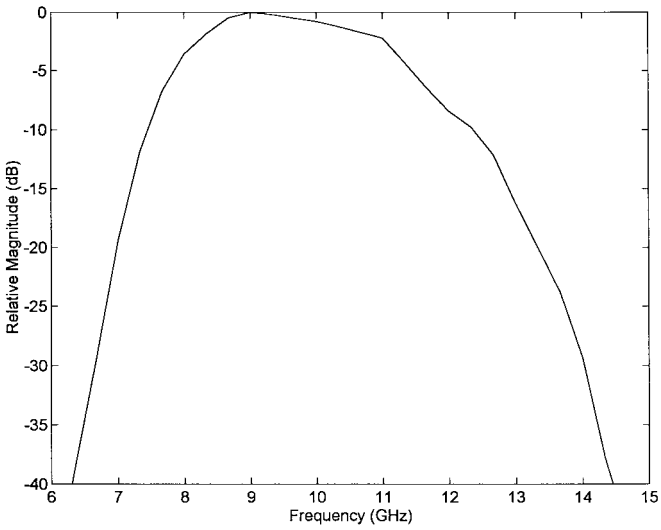

(b)

Fig. 2. (a) Microwave pulse generated the TWTA. Peak power level is approximately 1 kW. (b) RF spectrum of the pulse shown in (a).

Tecom Model 201821 horn (1.8–18 GHz). At 10 GHz, the azimuthal beamwidth of the horn is approximately 9° for vertical polarization and approximately 7° for horizontal.

Four dual-polarized Tecom antennas are used on the receive side of the system. In the experiments discussed in this paper, the horizontal and vertical ports of each antenna are followed by an RF amplifier (6–12 GHz) and a sampling head for a total of eight channels. However, this is not the primary mode of operation for the system. In its primary configuration, the system operates as a single-polarization imaging radar in which eight single-polarization antennas, rather than four dual-polarized elements, feed the eight acquisition channels. Azimuthal imaging is then achieved by time-domain beam forming, using the eight sampled waveforms. In this imaging configuration, the effective antenna-to-antenna spacing is 12.5 cm—half the spacing used in the polarimetric mode. While this wide spacing produces grating lobes, they are relatively weak since they lie outside the angular region illuminated by the transmit antenna. In the polarimetric mode utilized in this

paper, however, four dual-polarized antenna elements are used with a spacing of 25 cm and strong grating lobes limit the imaging capability. In this case, the four redundant antenna-amplifier-sampling-head chains are used primarily to improve the system signal-to-noise ratio (SNR) and to qualitatively investigate the spatial coherence of the backscatter, as discussed in Section IV.

The data acquisition system of the radar consists of a Tektronix 11801B sampling oscilloscope with an SM-11 multichannel expansion unit. Eight sampling heads are housed in the SM-11 to allow sampling of the outputs from each port of the four antennas. At each head, the microwave echo [such as the pulse seen in Fig. 2(a)] is sampled using equivalent time sampling. In equivalent time sampling, successive samples of the microwave echo are collected during successive pulse repetition intervals (PRI's). The range at which each successive sample is collected is increased by a small fraction of wavelength (typically 1.5 mm) between samples, allowing extremely high-effective sampling rates.

In the polarimetric mode, the system collects 2560 samples over a 3.84-m range swath. Assuming a PRI of 20 μs, 51.2 ms are required to complete each of these range scans. The data must thus be analyzed with care since decorrelation of the sea scatter across the full width of the swath may occur over this time period. Data collected in the near region of the swath may not be completely correlated with that from the far edge. However, samples for all four polarization combinations at a given range are collected within two PRI's (40 μs), and the time required to sample a pulse width (0.3 ns) is only 0.6 ms. Thus, while the equivalent time sampled echoes may not be completely correlated over the entire width of the swath, the waveform correlation length is nonetheless equal to many pulse widths, with its exact size dependent upon the value of the correlation time. If a correlation time of 10 ms is assumed, the waveform correlation length is approximately 500 samples, which equals 5.0 ns in equivalent time or 0.75 m in range. The actual correlation time of sea-scatter data with this degree of spatial resolution may be much longer, however, given that individual features on the surface are resolved. Plant *et al.* [21] have estimated the correlation time of X-band sea scatter at 45° grazing using field data collected in the North Sea and found a steady increase in this parameter from approximately 9 ms for a 40 m^2 illumination area to 14 ms for a patch size of 4 m^2. The scatterer lifetime implied by their data set is 60 ms. The illumination area for the UWB system in this paper is approximately 0.5 m^2 at a range of 60 m (10 m in azimuth by 0.05 m in range), an order of magnitude smaller than the smallest investigated by Plant.

Samples are initially stored in memory buffers within each head. Full buffers are off-loaded to an Exabyte tape via a GPIB interface controlled by a pc. Oscilloscope-to-pc transfer speeds allow one 3.84-m range scan by all eight heads every 1.5 s. All eight sampling heads are strobed simultaneously.

III. Experimental Setup and Environmental Conditions

During June 1996, the system was deployed on a research pier at the Coastal Engineering Research Center Field Research Facility (FRF), a research center for the Army Corps of Engineers in Duck, NC. The antennas were mounted on a rotatable pedestal at the end of the FRF pier at a height of 10.7 m above the mean water surface. Unobstructed views of the Atlantic off the North Carolina Outer Banks were allowed over azimuths from 340°N (along-shore) to approximately 90°N. The RF portion of the system electronics was housed in an enclosure beneath the pedestal while the pc and operator were stationed in a permanent laboratory approximately 20 m from the end of the pier. Fig. 3 contains a map indicating the position and orientation of the FRF pier with respect to the coastline. The mean water depth in the region where the data were collected is 7 m.

A relative calibration of the VV and HH radar channels was performed using several floating trihedral corner reflectors mounted on guard buoys in the area. Backscatter from the reflectors was collected over 15-min periods, averaged, and then compared with a standard multipath model in order to calibrate the magnitude of the two channels. Multiple runs indicate calibration to within 1 dB. As this is fundamentally a time-domain system, an approximate "phase" calibration was performed by balancing (through post-processing) the propagation time through the eight receive channels and by physically matching the cable lengths on the transmit side. While not as rigorous as the UWB polarimetric calibration technique described by Sletten [22], it is quite adequate for the purposes of this paper where only an approximate balance (within 20 ps) in the time of arrival of the VV and HH echoes is needed.

On June 23, 1996, backscatter was collected from an undeveloped sea containing a significant number of breaking waves. Data was collected at 10°, 20°, and 30° grazing, at corresponding ranges of 60, 30, and 21 m. Fig. 4 shows the wind speed and direction during the data collection as measured by FRF instruments mounted on the seaward end of the pier at a height of 19 m above the sea surface. The 10° and 20° data were collected between 1019 and 1116 EST when the wind speed was approximately 7 m/s. The 30° data was collected later, between 1413 and 1448 EST, when the wind speed had dropped to approximately 5 m/s. As shown in Fig. 4(b), the wind direction shifted steadily from approximately 0°N to 60°N over this period. In order to keep an upwind radar look direction, the pedestal was manually rotated as the wind shifted.

The significant wave height over the measurement period is plotted in Fig. 5. This data was collected by an FRF pressure gauge deployed approximately 500 m NE of the radar. The significant wave height is defined as four times the standard deviation of the surface elevation and is roughly equal to one-half the trough to crest height of the higher waves. Although this plot shows that the mean wave height grew steadily as the day progressed, it was observed visually that the frequency of wave breaking decreased somewhat as the wind speed fell. Breakers were most prevalent between 1000 and 1200 EST, during the strongest winds. Breaking also occurred during the collection of the 30° data, although it was somewhat less frequent.

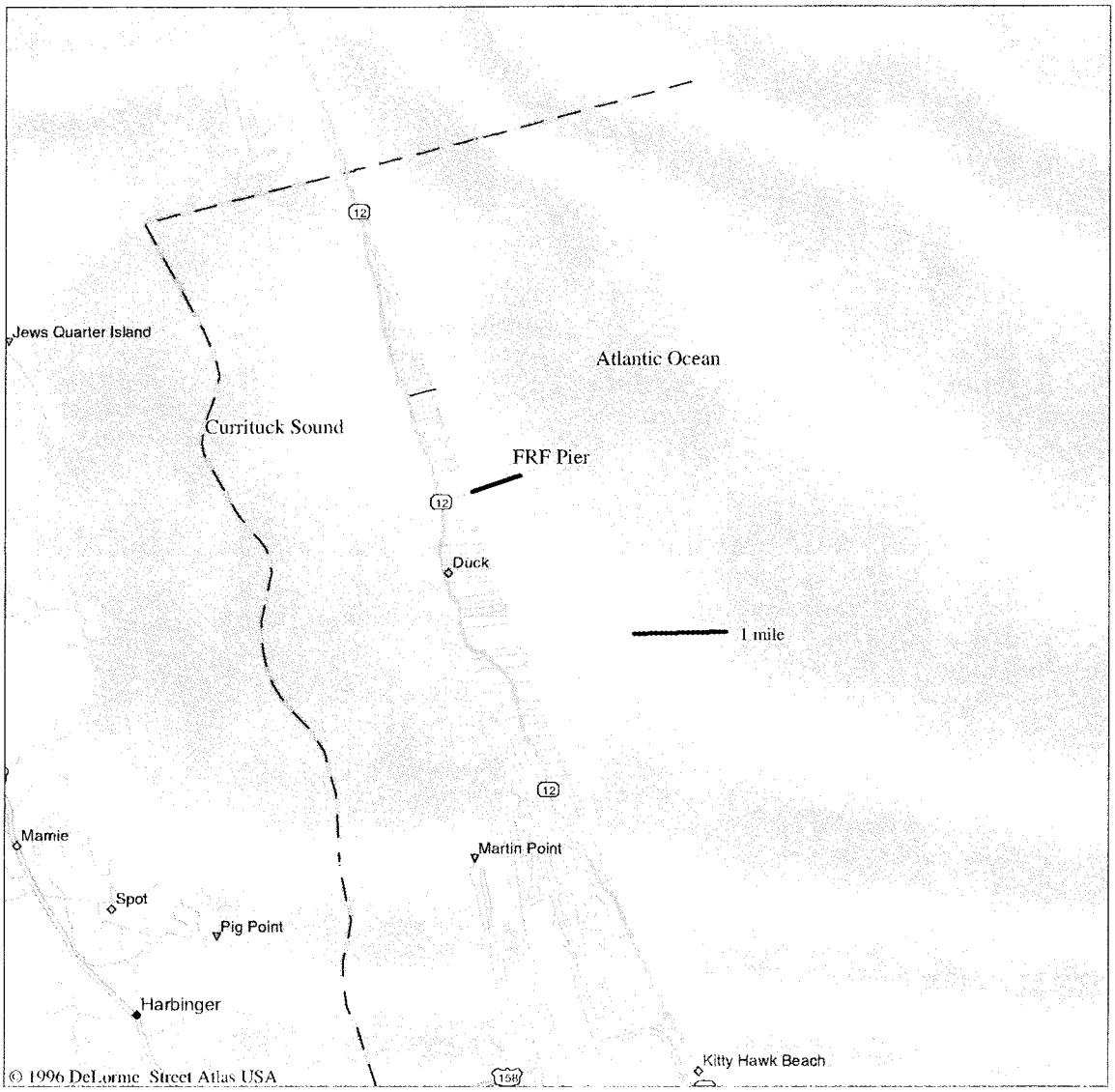

Fig. 3. Map of the North Carolina Outer Banks near Duck, NC, showing the position and orientation of the FRF pier.

IV. Data Analysis

This section presents the cumulative distribution functions (CDF's) for the data as well as the polarization ratios and RF spectra for the strongest echoes.

A. Cumulative Distribution Functions

The CDF's presented in this section were computed in the following manner. Each 3.84 m (25.6 ns) record was first filtered with a 6–12 GHz finite impulse response filter. The records were then divided into 4.5 cm (0.3 ns) bins with 50% overlap between adjacent bins. After tapering with a Hanning window, the fast Fourier transform (FFT) of the data within each bin (approximately 30 points) was then computed, and the complex amplitude of the transform at 9 GHz was taken as a measure of the bin signal amplitude and phase. (Since it is the peak of the transmitted spectrum, 9 GHz was chosen to represent the signal.) A normalized histogram of the amplitude was then computed and integrated to form a CDF.

The CDF's in this paper are plotted on Rayleigh probability paper, a log–log format, scaled such that Rayleigh distributed data will appear as a straight line with a slope of one. Variables with Weibull distributions also appear linear on Rayleigh paper, but may have other values of the slope. The probability density function (PDF) for a variable a with a Weibull distribution is given by

$$p(a) = (\nu a^{\nu-1}/\beta^{\nu}) \exp[-(a/\beta)^{\nu}]. \quad (1)$$

The parameter ν is referred to as the slope parameter. The Rayleigh distribution PDF is a special case of (1) for which $\nu = 2$.

The CDF's of the VV data can be seen in Fig. 6 along with the CDF of the system noise. As shown, 90% or more of the data appears to be well represented by a single Weibull distribution. Fitting a line to the CDF's between 10% and 90% produces slope parameters of 1.69, 1.70, and 1.85 for the 30°, 20°, and 10° data, respectively. Particularly in the 30° case, however, a significant deviation from linearity can be seen in

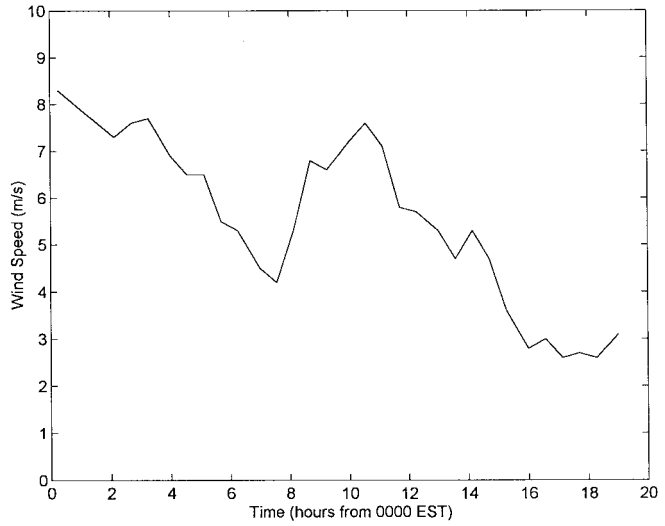

(a)

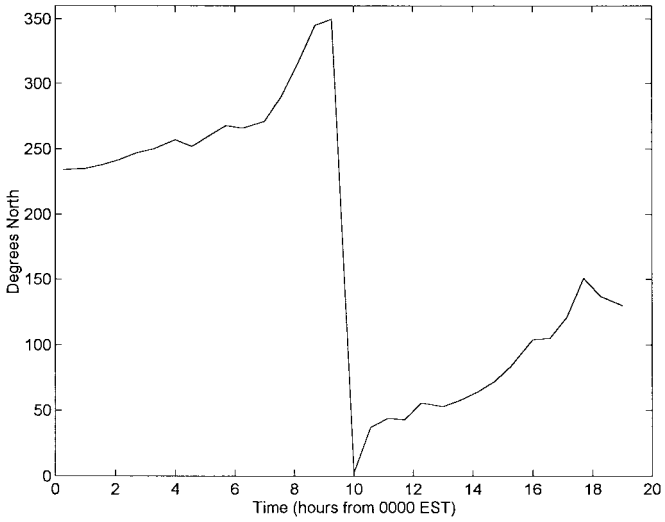

(b)

Fig. 4. (a) Wind speed during the data collection interval as measured by an FRF anemometer mounted on the seaward end of the pier. (b) Wind direction during the data collection interval.

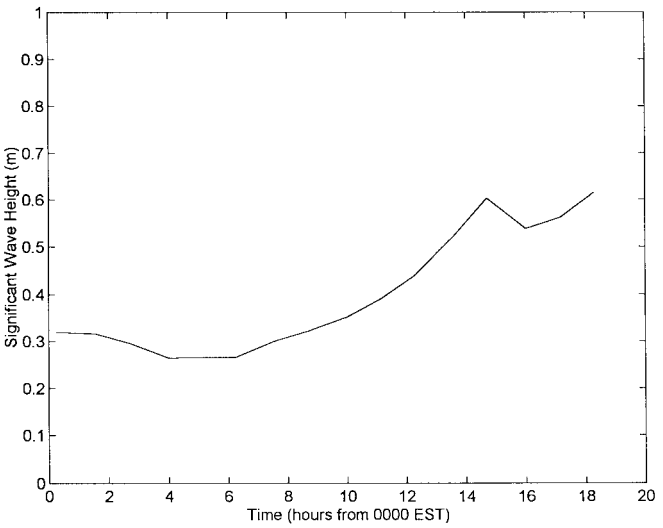

Fig. 5. Significant wave height during the data collection interval as measured by an FRF pressure gauge located approximately 500 m northeast of the seaward end of the FRF pier.

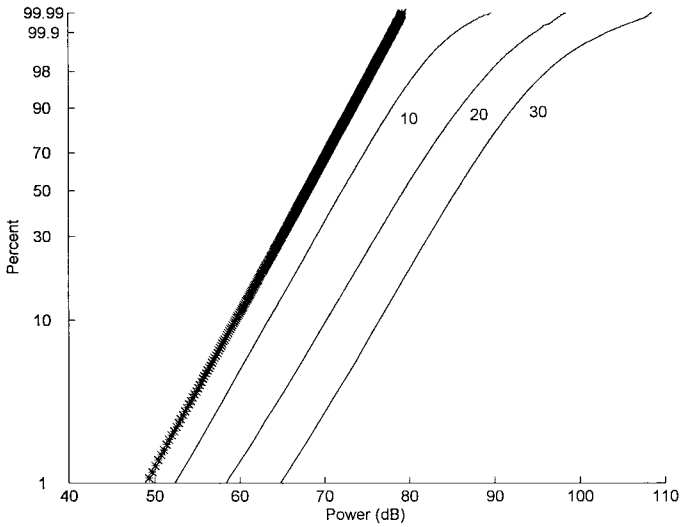

Fig. 6. Cumulative distribution functions for VV polarization at 30°, 20°, and 10° grazing angles. The CDF of the system noise is plotted as a cross-hatched line.

the strongest 5% of the data. The slope of the curve decreases, approaching a value corresponding to $\nu = 0.62$, although the identification of a second linear region is debatable. It should also be noted that the SNR is low for much of the data and, thus, the lower segments of the CDF's are governed more by the noise than the signal. A Weibull distribution with $\nu = 1.94$ fits the system noise very well, indicating essentially Rayleigh statistics.

The decrease in signal level with decreasing grazing angle is due, at least in part, to the increase in range to the sea surface. As noted earlier, the range to the surface is 60, 30, and 21 m for the 30°, 20°, and 10° data, respectively. Assuming a (distributed clutter) range fall off of r^3, this increase in range should incur decreases of 4.6 and 13.7 dB in the 20° and 10° data, respectively, relative to the data from 30°. The observed signal decreases are approximately 6 and 14 dB, respectively, in the lower power region, but the apparent fall off of the 10° data is limited by the system noise. The fall off with range approaches 8 and 18 dB, respectively, in the high-power tail. An r^4 fall off (point scatterer) would produce signal strength reductions of 6.2 and 18.2 dB at these ranges. Approximately 300 000 samples were used to generate each of the cdfs for 30° and 10°, and approximately 130 000 were used in the 20° case. This represents continuous operation of the radar system for approximately 30 and 15 min, respectively.

Fig. 7 contains the CDF's of the HH data. For each of the three grazing angles, the CDF is dominated by a lower amplitude, linear region extending up to the 90–95% level. The Weibull slope parameters which best describe these regions are 1.50, 1.71, and 1.85 for the 30°, 20°, and 10° curves, respectively. System noise is clearly dominating the 10° and 20° CDF's, as can be seen by comparing with the noise distribution. (There is an uncertainty on the order of 1 dB in the mean value of the system noise due to slow drift in the gain

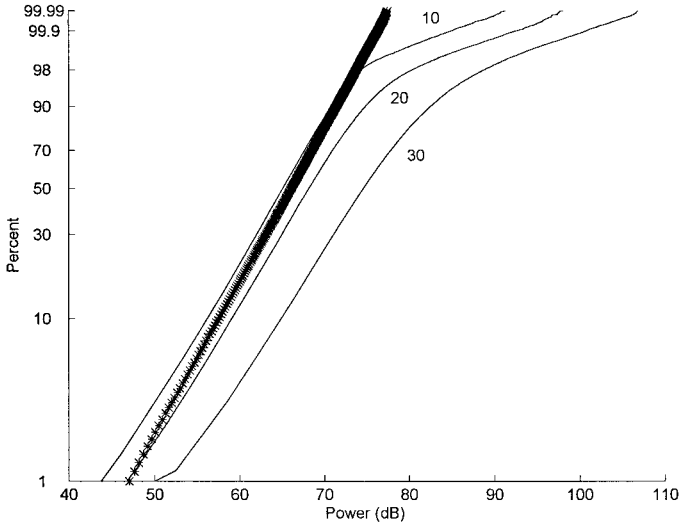

Fig. 7. Cumulative distribution functions for HH polarization at 30°, 20°, and 10° grazing angles. The CDF of the system noise is plotted as a cross-hatched line.

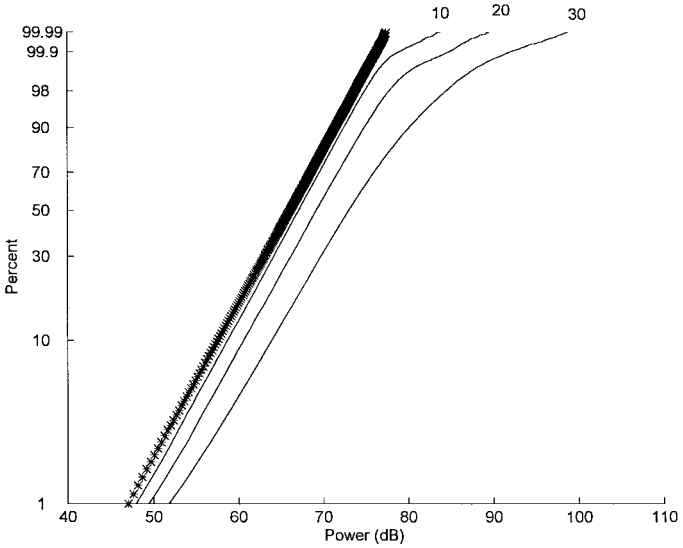

Fig. 8. Cumulative distribution functions for cross polarization at 30°, 20°, and 10° grazing angles. The CDF of the system noise is plotted as a cross-hatched line.

of the receive amplifiers.) However, each curve also exhibits a second, higher amplitude region in the uppermost 5% with a significantly lower slope. The Weibull slope parameters for these regions are 0.39, 0.39, and 0.43, respectively, for 30°, 20°, and 10°. The range fall off of the HH data appears somewhat closer to r^4 than r^3 as the upper regions of the 20° and 10° curves are displaced from the 30° data by approximately 8 and 16 dB, respectively.

The cross-polarized (VH or HV) data is presented in Fig. 8. The CDF's are similar in shape to the HH-polarized data, but the break between the upper and lower regions occurs at a higher percentile. The range fall off in the tail region is similar to that seen in the HH data, with the 20° and 10° data approximately 8 and 15 dB, respectively, below the 30° curve.

B. Polarization Ratio of the Strongest HH Echoes

Fig. 9 illustrates a trend in the polarization ratio of the strongest echoes. (In this paper, the ratio is defined as the ratio of the HH power divided by the corresponding VV power.) Fig. 9(a) is a histogram of the polarization ratio values for the strongest 1% of the HH samples collected at 30° grazing. The geometric mean (average over polarization ratio values in decibels) is −1.4 dB, while the ratio of the mean HH power to mean VV power is −2.2 dB. As seen in Fig. 9(c), decreasing the grazing angle to 10° increases the geometric mean to 3.6 dB, while the ratio of the mean HH and VV power levels shifts up to 1.7 dB. The data at 20° [Fig. 9(b)] fall between the 30° and 10° values with a geometric mean of −0.1 dB, and a ratio of mean HH to mean VV powers of −1.2 dB. There also appears to be an increase in the width of the 10° distribution relative to that at 30°.

The strongest 1% of the HH echoes were chosen for this analysis to minimize the effect of the system noise and to focus the analysis on scattering events with the strong HH backscatter characteristic of sea spikes. A similar analysis applied to the strongest 1% of the VV echoes reveals a *decrease* of approximately 5 dB in the geometric mean of the polarization ratio (−8.8 to −13.8 dB), and a 2-dB decrease in the mean HH to mean VV signal strength ratio (−4.7 to −6.5 dB) as the grazing angle decreases from 30° to 10°.

C. Spectral Analysis of the Strongest HH Echoes

The results presented thus far reflect the ultrahigh resolution of the UWB system, but have not yet addressed variations that may be present in the RF frequency content of the data. This section presents the RF waveforms and spectra of a representative sample of the strongest echoes, those comprising the strongest 1%. The spectra were generated by first centering an analysis window around the echo of interest, applying Hanning tapering, and then performing an FFT. A 0.5-m (3.3-ns) wide analysis window has been used, which produces a frequency resolution of 0.15 GHz.

Fig. 10 shows typical VV and HH sea-spike waveforms observed at 10° and their corresponding spectra. As seen in Fig. 10(a), the HH echo has approximately twice the amplitude of the VV signal and is more localized in range. The VV waveform lacks the coherent appearance of the HH signal, having a more broken appearance with several phase breaks. The HH spectral shape shown in Fig. 10(b) is distinctive and is common at this grazing angle. Two peaks are visible with a separation of approximately 2 GHz. Two main peaks are also visible in the VV spectra, but the response is not as smooth across the band as a result of the lesser degree of coherence in the waveform. Fig. 11 illustrates this characteristic with another example. Fig. 11(a) shows the four VV and HH waveforms collected by the four antennas in the receive antenna array, in order, moving from element to element across the array. The VV waveforms vary significantly, although the general location of the envelope does not, while the HH echo shape changes relatively little. This is reflected in the coherence of the corresponding spectra, shown in Fig. 11(b) and (c). (Note the two peaks again in the HH spectra.) This difference in the coherence of the VV and HH waveforms

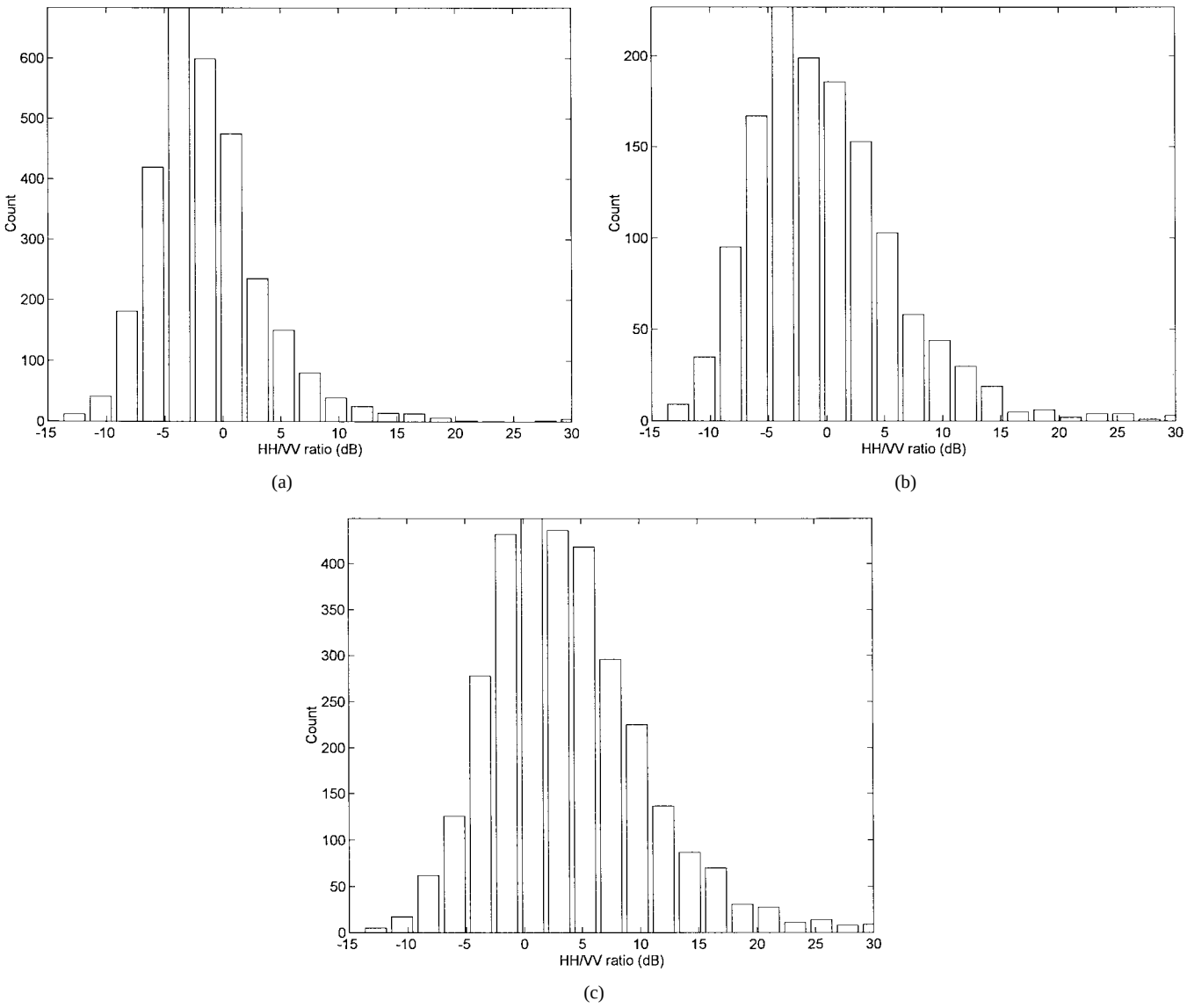

Fig. 9. Polarization ratio (HH/VV) histograms for the strongest 1% of the HH polarized samples. (a) 30° grazing. (b) 20° grazing. (c) 10° grazing.

across the receive array is probably due to a difference in the number of significant scatterers. The HH echo appears to originate from a single localized scattering center, whereas the look-angle sensitivity of the VV echo can be explained by the presence of a number of spatially separated scatterers. A third example of a strong 10° spike is shown in Fig. 12. This example is notable due to the shape of the HH waveform. Three distinct contributions to the echo are visible with a spatial separation of about 7.5 cm (0.5 ns) and the overall waveform has a smooth, Gaussian-like envelope. Also notable are the complementary peaks and nulls in the VV and HH spectra, shown in Fig. 12(b). Note that the HH spectrum is similar to that for the previous two examples, although the details of the waveforms differ.

Representative examples from the strong 30° grazing-angle spikes can be seen in Figs. 13–15. In Fig. 13, both waveforms are well defined with the VV signal approximately 2.5 dB stronger than the HH. Fig. 14 shows an example in which the VV and HH echoes are nearly identical in shape, but with the VV signal approximately 5 dB greater than the HH. Both spectra exhibit two peaks with a separation of approximately 2 GHz. A third example can be seen in Fig. 15. As shown in Fig. 15(a), the waveforms in this example vary appreciably across the array, but corresponding VV and HH echoes remain similar to one another. Both VV and HH polarizations exhibit similar spectra with a deep null near 9 GHz [Fig. 15(b)].

V. Discussion

A. Cumulative Distribution Functions

Qualitatively, the CDF's shown in Figs. 6 and 7 bear some resemblance to those from previous high-resolution clutter studies. For instance, Hansen and Caveleri [2] and Olin [3] measured X-band clutter under sea state two conditions at a grazing angle of 3° and found that upwind VV statistics were essentially Rayleigh, but that the HH data deviated from Rayleigh statistics in the upper 10%. In this upper region, a Weibull slope parameter of approximately 0.5 described the

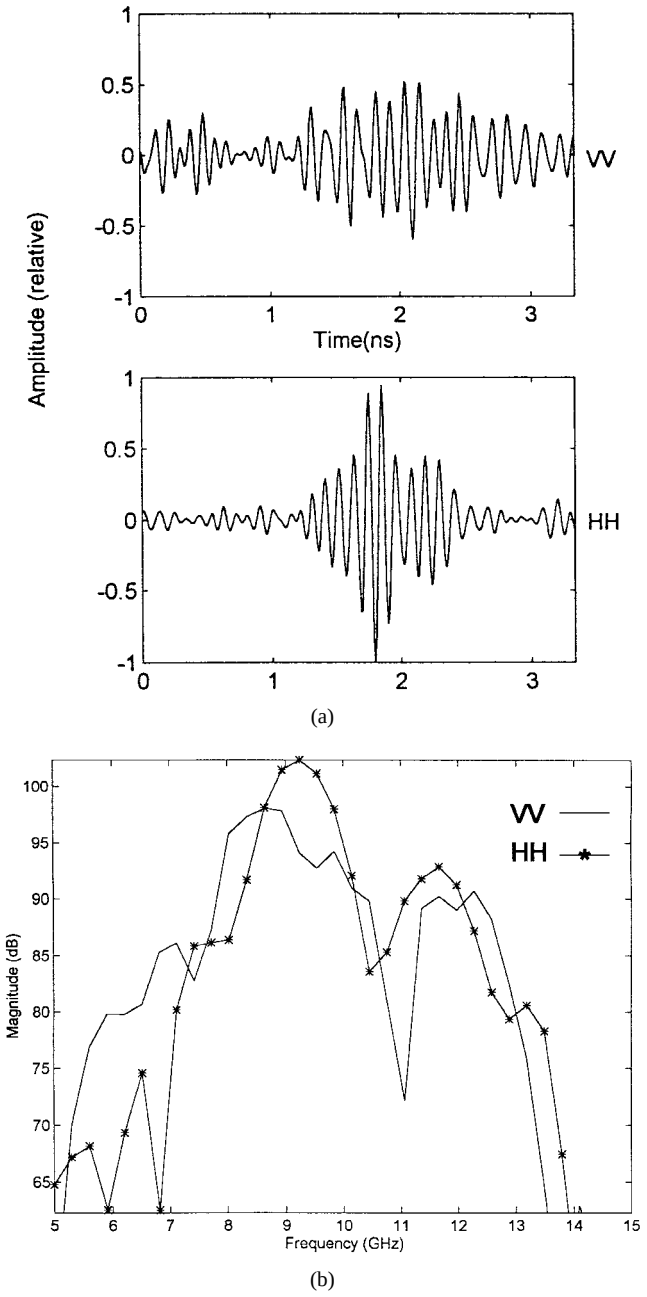

Fig. 10. (a) VV and HH waveforms for a typical strong sea spike at a grazing angle of 10°. HH waveforms are typically more localized and better defined than the corresponding VV waveforms. (b) RF spectra for the waveforms shown in (a).

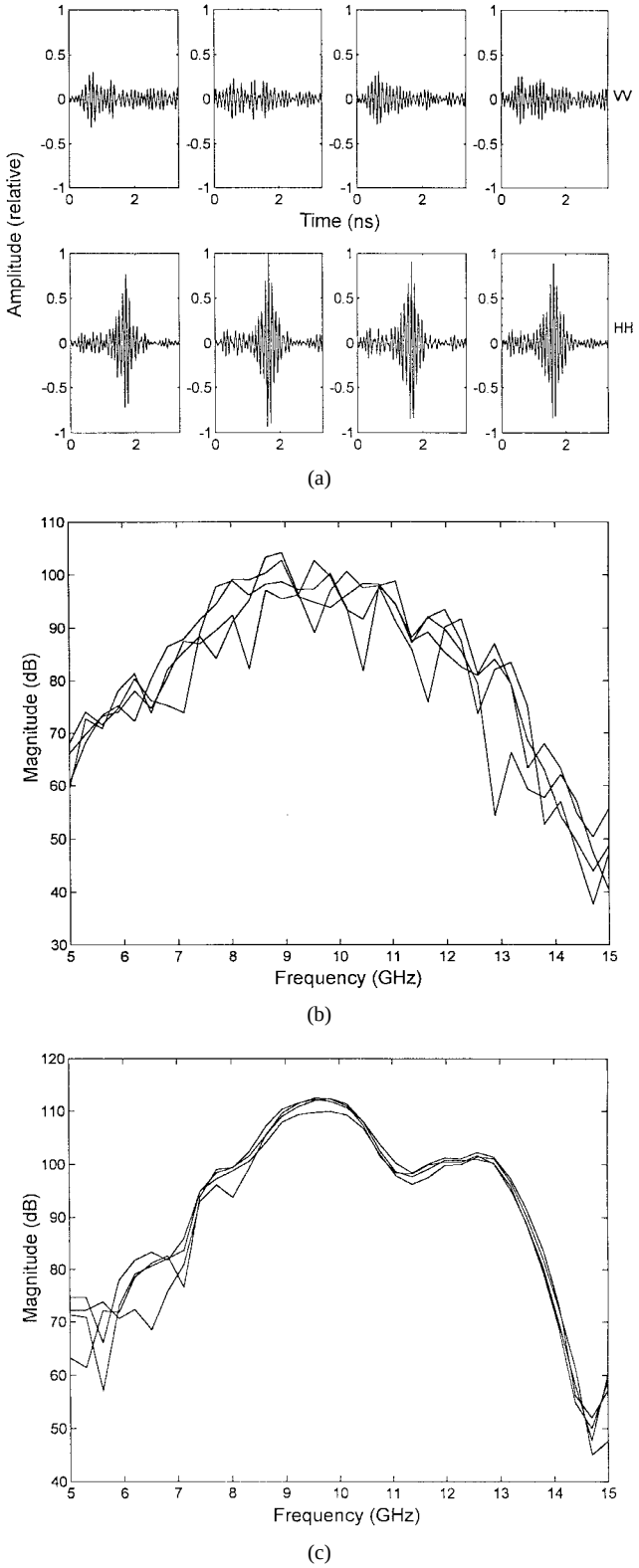

Fig. 11. (a) VV and HH polarized waveforms recorded by each of the four elements of the receive antenna array (in order, from left to right) at a grazing angle of 10°. The strong HH echoes typically vary little across the array, whereas the corresponding VV echoes may change appreciably. (b) RF spectra of the VV waveforms shown in (a). (c) RF spectra of the HH waveforms shown in (a).

CDF. At sea state five, these authors report a Weibull slope parameter near 0.6 for HH polarization. The HH CDF's in this paper are characterized by slope parameters near 0.4 in the high-amplitude tails and thus indicate even broader distributions. Baker [23] and Hair *et al.* [24] have also measured high-resolution clutter statistics at low-grazing angles and have successfully modeled their results using the K distribution. However, a quantitative comparison of their results with the data presented here requires an additional analysis based on this compound Rayleigh–Chi distribution. Qualitatively, the CDF's in this paper also resemble curves for Ku-band data collected at 45° incidence by Gotwols and Thompson [25]. Their data also exhibit a significant deviation from simple Weibull statistics in the higher amplitude regions and the authors have developed a single compound PDF model that

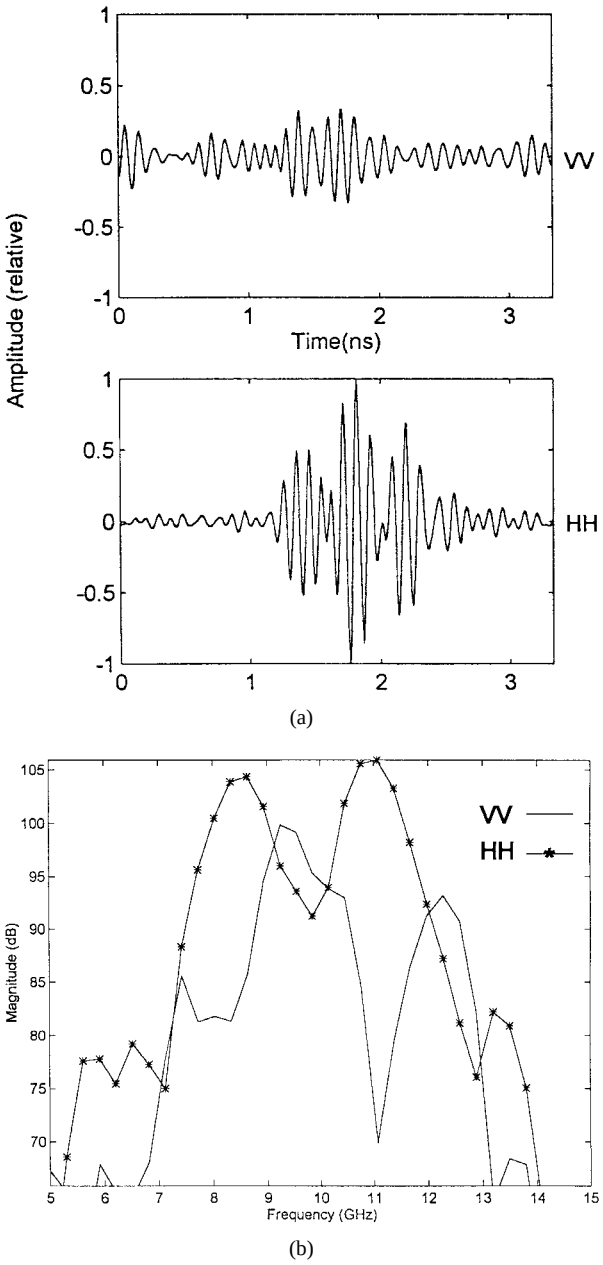

Fig. 12. (a) VV and HH polarized waveforms for a sea spike at 10°. The HH waveform can be interpreted as the sum of three spatially resolved components of a multipath echo. (b) RF spectra of the waveforms shown in (a).

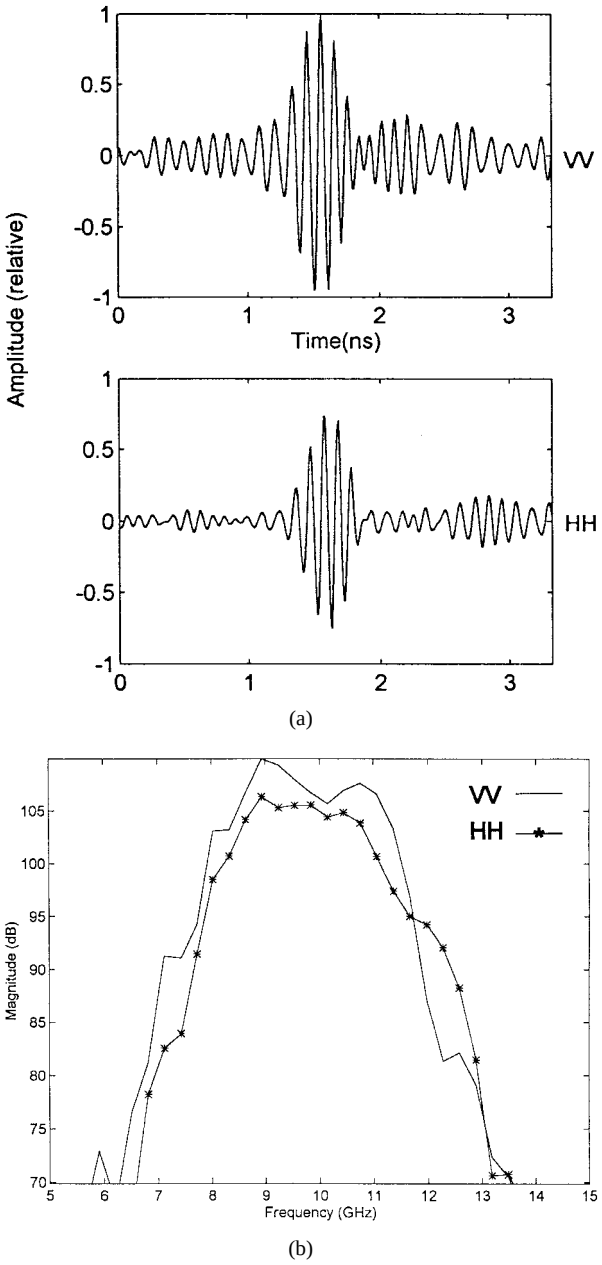

Fig. 13. (a) VV and HH waveforms for a typical strong sea spike at a 30° grazing angle. (b) RF spectra of the waveforms shown in (a).

describes the entire distribution. Unfortunately, comparisons cannot proceed much beyond this qualitative stage, since the low SNR of much of the data in the present paper precludes an unambiguous determination of the true clutter statistics, particularly in the case of the 20° and 10° measurements. An analysis of the type presented by Watts [26] is necessary before more quantitative comparisons can be made. The remainder of this paper will focus on scattering events comprising the tails of the VV and HH distributions, where the SNR is significantly higher.

B. Polarization Ratios of the Strongest HH Echoes

A feature-dominated model which incorporates the polarization sensitivity of the water surface can explain some of the characteristics of the polarization ratio histograms in Fig. 9. Consider a simple multipath scattering model for a breaking wave, as discussed in [14] and [19]. Assume a scattering center, such as a plume or sharp crest, on a breaking wave at some height h above the surface of the water. A standard multipath model predicts the following expression for the backscattered field:

$$E^{pp} = E_o^{pp}[S_{dd}^{pp} + 2R^p S_{di}^{pp} e^{jk2h \sin \varphi} + (R^p)^2 S_{ii}^{pp} e^{jk4h \sin \varphi}] \tag{2}$$

where p = V or H, depending on the polarization. Here, φ is the appropriate grazing angle, S_{dd}^{pp}, S_{di}^{pp}, and S_{ii}^{pp} are the direct–direct, indirect–direct, and indirect–indirect scattering coefficients for the scatterer, respectively. k is the radar wave number. R^p is the reflection coefficient of water, a strong

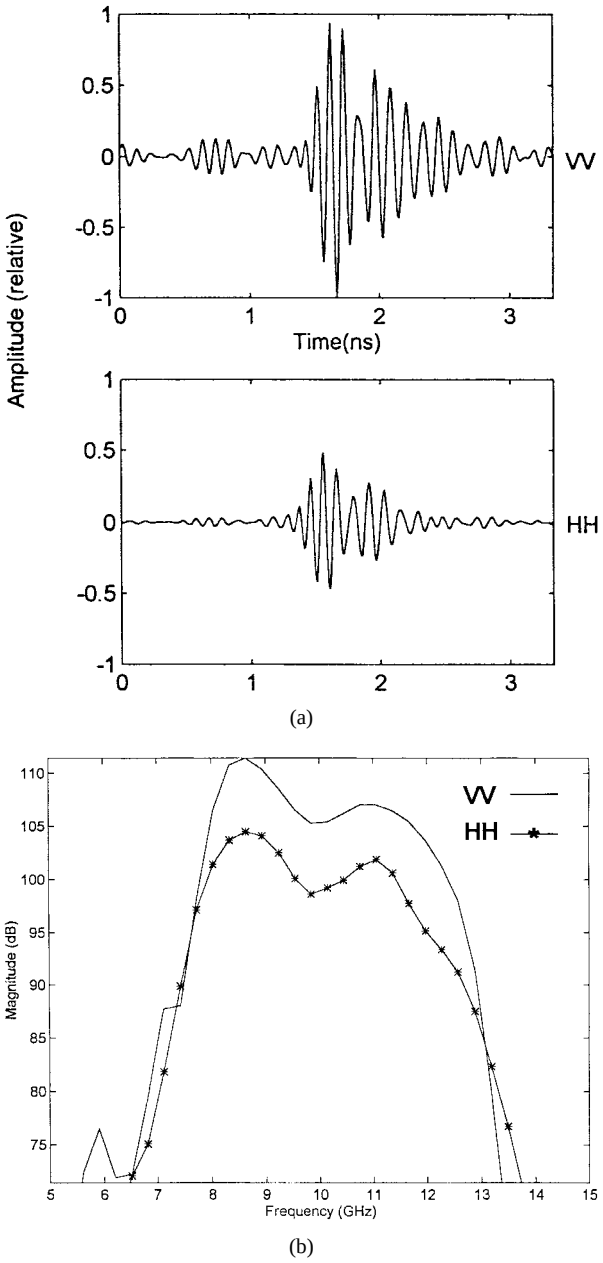

Fig. 14. (a) VV and HH waveforms for a typical strong sea spike at a 30° grazing angle. (b) RF spectra of the waveforms shown in (a).

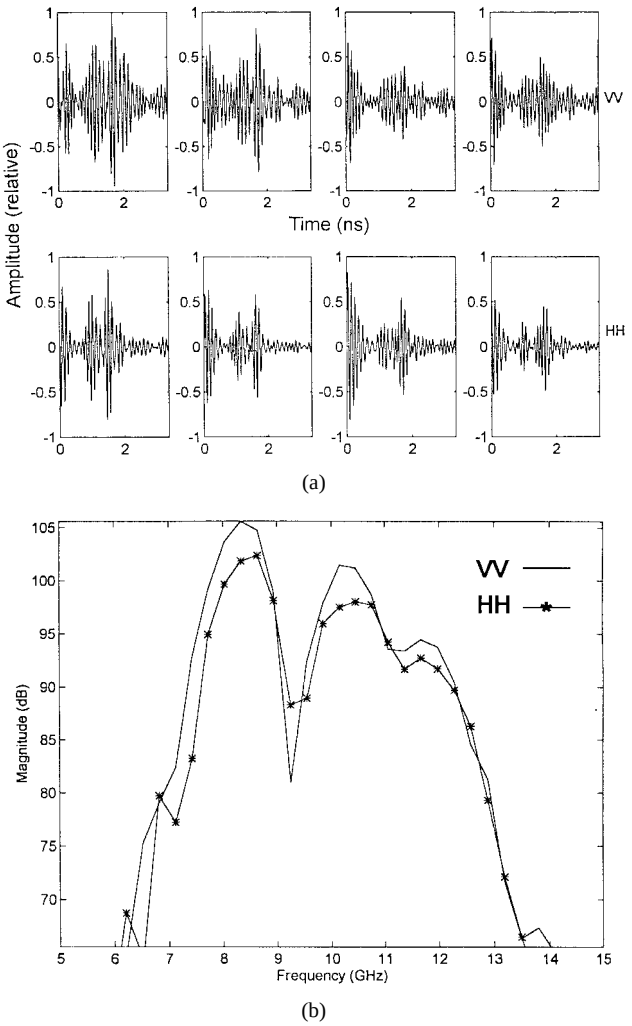

Fig. 15. (a) VV and HH polarized waveforms recorded by each of the four elements of the receive antenna array (in order, from left to right) at a grazing angle of 30°. The waveforms for both polarizations vary across the array, but remain similar to one another. (b) RF spectra of the leftmost VV and HH waveforms shown in (a).

function of grazing angle and polarization due to Brewster angle effects [27]. The path-length difference between the direct and indirect paths is

$$\Delta = 2h \sin \varphi. \tag{3}$$

As it stands, (2) predicts a wide range of signal amplitudes, depending on the exact height of the scatterer and the local grazing angle and is, in fact, very sensitive to small changes in the scatterer height. At 10 GHz and a 10° grazing angle, the direct–indirect exponential factor rotates through 2π radians in phase with only an 8.7 cm change in h, while the phase of the indirect–indirect term rotates at twice this rate. A more useful expression is obtained by determining the backscattered power (proportional to the square of the magnitude of this expression) and averaging over a range of expected scatterer heights and strengths. This produces the following expression:

$$\begin{aligned}\langle E^{pp} \cdot E^{pp^*} \rangle = E_o^{pp^2} \langle [& |S_{dd}^{pp}|^2 + 4|R^p|^2 |S_{di}^{pp}|^2 + |R^p|^4 |S_{ii}^{pp}|^2 \\ & + \text{terms involving } \cos(2kh \sin \varphi) \\ & \text{and } \cos(4kh \sin \varphi)] \rangle. \end{aligned} \tag{4}$$

In view of the sensitivity of the cosine terms to kh, the average of these terms vanishes over even a small range of scatterer heights. Taking the ratio of the mean HH and VV signal powers then produces the following expression for the mean polarization ratio:

$$\langle \chi \rangle = \frac{\langle |S_{dd}^{\mathrm{HH}}|^2 + 4|R^{\mathrm{H}}|^2 |S_{di}^{\mathrm{HH}}|^2 + |R^{\mathrm{H}}|^4 |S_{ii}^{\mathrm{HH}}|^2 \rangle}{\langle |S_{dd}^{\mathrm{VV}}|^2 + 4|R^{\mathrm{V}}|^2 |S_{di}^{\mathrm{VV}}|^2 + |R^{\mathrm{V}}|^4 |S_{ii}^{\mathrm{VV}}|^2 \rangle}. \tag{5}$$

Values for the scattering coefficients for breaking waves have yet to be calculated, so it is difficult to make quantitative comparisons of this model with experimental data. However, assuming these parameters do not vary drastically with grazing angle and that their amplitudes scale similarly with scatterer

strength, the variation of (5) with grazing angle can still be investigated. In lieu of better estimates, assume all coefficients have a relative value of one. (This may be a fairly accurate estimate if the scatterer is an overturning crest that supports a specular reflection in both the direct and indirect paths.) At grazing angles of 30°, 20°, and 10°, the water reflection coefficients at 9 GHz (the peak of the transmitted pulse spectrum) are $|R^{\mathrm{H}}| = 0.88$, 0.9, and 0.95 and $|R^{\mathrm{V}}| = 0.65$, 0.5, and 0.15, respectively [27]. Note that the Brewster angle for seawater is approximately 9° at 9 GHz. Substituting these values into (5) produces polarization ratios of 2.1, 3.8, and 7.0 dB, respectively. Thus, the model predicts an increase of approximately 5 dB in the mean polarization ratio as the grazing angle changes from 30° to 10°, in good agreement with the data presented in the previous section. Better estimates of the scattering coefficients are needed before this model can be investigated further. The model is presented here primarily to illustrate how multipath and the presence of a Brewster angle can explain the gross trends in the data.

Lee *et al.* [6] have also measured the polarization ratio over the 10°–30° grazing-angle range during experiments at Loch Linnhe and the Sound of Sleat in Scotland, but found the ratio for "fast" (i.e., non-Bragg) scatterers to be roughly constant with a value between -5 and -10 dB. The discrepancy between their results and those presented in this paper is not surprising, however, since Lee *et al.* did not restrict their calculations to only the strongest echoes, as is done in this paper, but rather included all samples within a specified Doppler frequency band. Also, although the wind speed was comparable in the two experiments, the surface wave fields were quite different. For instance, the waves were short in the Scottish experiments, with a dominant wave frequency between 0.45 and 0.7 Hz, while the dominant wave frequency was approximately 0.11 Hz during this North Atlantic experiment.

C. Spectral Analysis of the Strongest HH Echoes

The waveform shapes and spectra also strongly suggest a multipath scattering mechanism. The peaks and nulls in the spectra and the distinct VV and HH waveforms shown in Figs. 10–12 are also seen in laboratory wavetank data, as reported by Sletten and Wu [8]. In their laboratory experiments, the authors measured the backscatter at 10° grazing from spilling breakers using a polarimetric UWB radar similar to the system employed here. West and Sletten [13] have recently simulated these laboratory measurements, and the dominance of multipath in the scattering mechanism has been verified. Through numerical simulation and measurements of a perfectly conducting bench-top model, the authors showed that the peaks and nulls in the spectra are interference fringes caused by interactions between direct echoes from a small plume near the breaker crest and echoes that also experience one or more reflections off the front face or trough of the wave. In the bench-top model measurements, the VV and HH peaks and nulls were found to be complementary, a characteristic attributed to the 180° phase difference in the vertically and horizontally polarized forward reflection coefficients for a perfect conductor. For similar reasons, the VV and HH spectra for the wavetank breakers were also found to be roughly complementary. The VV and HH spectra for some of the 10° echoes presented here also exhibit this characteristic, notably the data in Fig. 12(b). The HH waveform in this figure certainly suggests multipath. The three "subechoes" have the proper relative amplitudes and spacing: a direct–direct echo, followed by a direct–indirect echo with twice the amplitude, and finally an indirect–indirect echo. The 30° spectra in Figs. 13–15 also indicate multipath through the presence of maxima and minima although, in general, the VV and HH waveforms and spectra are more alike than different. This may be a result of the closer match in the vertical and horizontal water reflection coefficients at this angle and a stronger specular character to the plume scattering mechanism as the measurement moves out of the grazing incidence regime.

Assuming multipath is the cause of the spectral peaks, the peak spacing is indicative of the path length difference between the interfering components that comprise the echo. In the simplest case of two-component multipath, the peaks, which are interference fringes, occur at those frequencies satisfying

$$\Delta = n \cdot \lambda = n \cdot \frac{c}{f} \tag{6}$$

where Δ is the path-length difference given by (3), n is the order of the fringe, λ is the radar wavelength, f the corresponding frequency, and c the speed of light. If two successive fringes (n and $n+1$) can be identified at frequencies f_1 and f_2, the order can be deduced by eliminating Δ and computing

$$n = \frac{f_1}{f_2 - f_1}. \tag{7}$$

Applying this analysis to the HH spectrum in Fig. 10, with $f_1 = 9.2$ GHz and $f_2 = 11.5$ GHz, produces an order $n = 4.0$. Encouraged by the fact that this analysis produces an integer order, one can then proceed to solve (3) and (6) for h and calculate a scatterer height of 0.37 m, in reasonable agreement with the significant wave height. Not all of the spectra produce integer values of n when this analysis is applied, however, implying that the scattering process generally involves more than just two interfering components. The peaks in the other 10° spectra shown in this paper infer orders of 3.2, 3.4, and 5.3, which, when rounded to the nearest integer, correspond to h values of 0.27, 0.3, and 0.54 m, respectively. Trizna and Carlson [28] also applied a multipath model to sea-scatter data and from it estimated scatterer heights on the order of 4 cm, but a fringe order $n = 1$ was assumed. Here, the order is inferred from the data itself.

VI. Summary

This paper presents UWB polarimetric sea-scatter measurements conducted from a research pier located on the Outer Banks of North Carolina. Data was collected at grazing angles of 30°, 20°, and 10° under wind speeds between 5 and 7 m/s. Cumulative distribution functions of the data indicate that below the 90th percentile, both VV and HH CDF's are represented well by Weibull distributions with slope

parameters ranging from 1.5 to 1.85. However, the highest 5–10% of the samples follow a distribution with a much broader tail, corresponding to a Weibull slope parameter near 0.4 for horizontal polarization. The mean polarization ratio of the strongest HH spikes is computed and compared across the three grazing angles, and a rise of approximately 5 dB is observed as the grazing angle decreases from 30° down to 10°. A simple model for multipath scattering from a breaking wave is used to attribute this decrease to Brewster angle effects. An analysis of the RF waveforms and spectra for the strong spikes also indicates that multipath plays an important role in the generation of these events. The waveforms for VV and HH polarizations differ substantially, at least in the 10° case, and peaks appear in the RF spectra which are similar to interference fringes previously observed in the UWB frequency response of wavetank breaking waves. The multipath model is used to extract information on the order of these apparent interference fringes and, from this, an estimate of the scatterer height above the surface is made which agrees reasonably well with *in situ* measurements of the sea surface.

ACKNOWLEDGMENT

The author would like to thank Dr. F. Herr and Dr. D. Trizna of the Office of Naval Research, Arlington, VA, managers of the Mine Surface Effects Program, under which this UWB radar system was developed. He would also like to thank Dr. B. Gotwols of the Johns Hopkins Applied Research Laboratory, Baltimore, MD, for his helpful suggestions regarding the probability distribution functions, and the staff of the Coastal Engineering Research Center FRF for their assistance during the deployment and for the use of the meteorological and surface-wave data.

REFERENCES

[1] D. J. McLaughlin, N. A. Allen, L. M. Twarog, and D. B. Trizna, "High resolution polarimetric radar scattering measurements of low grazing angle sea clutter," *IEEE J. Oceanic Eng.*, vol. 20, pp. 166–178, July 1995.

[2] J. P. Hansen and V. F. Cavaleri, "High resolution radar sea scatter, experimental measurements and discriminants," Naval Res. Lab., Washington, DC, Rep. 8557, 1982.

[3] I. D. Olin, "Amplitude and temporal statistics of sea spike clutter," in *Int. Conf. Radar*, London, U.K., Oct. 1982, pp. 198–202.

[4] D. B. Trizna, "Statistics of low grazing angle radar sea scatter for moderate and fully developed ocean waves," *IEEE Trans. Antennas Propagat.*, vol. 39, pp. 1681–1690, Dec. 1991.

[5] M. J. Smith, E. M. Poulter, and J. A. McGregor, "Doppler radar measurements of wave groups and breaking waves," *J. Geophys. Res.*, vol. 101, no. C6, pp. 14269–14282, June 1996.

[6] P. H. Y. Lee, J. D. Barter, K. L. Beach, C. L. Hindman, B. M. Lake, H. Rungaldier, J. C. Shelton, A. B. Williams, R. Yee, and H. C. Yuen, "X-band microwave backscattering from ocean waves," *J. Geophys. Res.*, vol. 100, pp. 2591–2611, Feb. 1995.

[7] A. D. Rozenberg, D. C. Quigley, and W. K. Melville, "Laboratory study of polarized scattering by surface waves at grazing incidence: Part I—Wind waves," *IEEE Trans. Geosci. Remote Sensing*, vol. 33, pp. 1037–1046, July 1995.

[8] M. A. Sletten and J. Wu, "Ultrawideband, polarimetric radar studies of breaking waves at low grazing angles," *Radio Sci.*, vol. 31, no. 1, pp. 181–192, Jan./Feb. 1996.

[9] N. Ebuchi, H. Kawamura, and Y. Toba, "Physical processes of microwave backscattering from laboratory wind wave surfaces," *J. Geophys. Res.*, vol. 98, no. C8, pp. 14669–14681, Aug. 1993.

[10] D. B. Trizna, J. P. Hansen, P. A. Hwang, and J. Wu, "Laboratory studies of radar sea spikes at low grazing angles," *J. Geophys. Res.*, vol. 96, no. C7, pp. 12529–12537, July 1991.

[11] E. G. Eckert, C. L. Rino, A. Siegal, and T. Webster, "Ocean microwave backscatter from the LOGAN experiment," in *Proc. Int. Geosci. Remote Sensing Symp. (IGARSS'94)*, Pasadena, CA, Aug. 1994, pp. 815–817.

[12] A. T. Jessup, W. C. Keller, and W. K. Melville, "Measurements of sea spikes in microwave backscatter at moderate incidence," *J. Geophys. Res.*, vol. 95, no. C6, pp. 9679–9688, June 1988.

[13] J. C. West and M. A. Sletten, "Multipath EM scattering from breaking ocean waves at grazing incidence," *Radio Sci.*, vol. 32, no. 4, pp. 1455–1467, July/Aug. 1997.

[14] D. B. Trizna, "A model for Brewster angle damping and multipath effects on the microwave radar sea echo at low grazing angles," *IEEE Trans. Geosci Remote Sensing*, vol. 35, pp. 1232–1244, Sept. 1997.

[15] S. G. Hanson and V. U. Zavorotny, "Polarization dependency of enhanced multipath radar backscattering from an ocean-like surface," *Waves Random Media*, vol. 5, pp. 159–165, 1995.

[16] D. R. Lyzenga, A. L. Maffett, and R. A. Shuchman, "The contribution of wedge scattering to the radar cross section of the ocean surface," *IEEE Trans. Geosci. Remote Sensing*, vol. GRS-21, pp. 502–505, Oct. 1983.

[17] L. B. Wetzel, "Models for electromagnetic scattering from the sea at extremely low grazing angles," Naval Res. Lab., Washington, DC, Rep. 6098, Dec. 1987 (available from NTIS as ADA 190-472).

[18] M. A. Sletten and D. B. Trizna, "An ultrawideband, polarimetric radar for the study of sea scatter," *IEEE Trans. Antennas Propagat.*, vol. 42, pp. 1461–1466, Nov. 1994.

[19] M. A. Sletten, D. B. Trizna, and J. P. Hansen, "Ultrawide-band radar observations of multipath propagation over the sea surface," *IEEE Trans. Antennas Propagat.*, vol. 44, pp. 646–651, May 1996.

[20] J. P. Hansen "A system for performing ultra-high resolution backscatter measurements of splashes," in *Proc. IEEE Int. Microwave Theory Tech. Symp.*, New York, 1986, pp. 633–636.

[21] W. J. Plant, E. A. Terray, R. A. Petitt, and W. C. Keller, "The dependence of microwave backscatter from the sea on illuminated area: Correlation times and lengths," *J. Geophys. Res.*, vol. 99, no. C5, pp. 9705–9723, May 1994.

[22] M. A. Sletten, "Resolution of a phase ambiguity in a calibration procedure for polarimetric radar systems," *IEEE Trans. Geosci. Remote Sensing*, vol. 32, pp. 213–216, Jan. 1994.

[23] C. J. Baker, "K-distributed coherent sea clutter," *Proc. Inst. Elect. Eng.*, vol. 138, pt. F, no. 2, Apr. 1991.

[24] T. Hair, T. Lee, and C. J. Baker, "High range-resolution sea reflections," *Proc. Inst. Elect. Eng.*, vol. 138, pt. F, no. 2, Apr. 1991.

[25] B. L. Gotwols and D. R. Thompson, "Ocean microwave backscatter distributions," *J. Geophys. Res.*, vol. 99, no. C5, pp. 9741–9750, May 1994.

[26] S. Watts, "Radar detection prediction in K-distributed sea clutter and thermal noise," *IEEE Trans. Aerosp. Electron. Syst.*, vol. AES-23, pp. 40–45, Jan. 1987.

[27] D. E. Kerr, Ed., *Propagation of Short Radio Waves*. New York: McGraw-Hill, 1951.

[28] D. B. Trizna and D. J. Carlson, "Studies of dual polarized low grazing angle radar sea scatter in nearshore regions," *IEEE Trans. Geosci. Remote Sensing*, vol. 34, pp. 747–757, May 1996.

Mark A. Sletten (S'87–M'91) received the B.S., M.S., and Ph.D. degrees in electrical engineering from the University of Wisconsin, Madison, in 1984, 1987, and 1991, respectively.

From 1985 to 1987, he was a Research Assistant and ECE Department Fellow at the Wisconsin Center for Applied Microelectronics, Madison, WI, involved in the development of optical detectors and held internships at Hewlett Packard's integrated circuit research facility in Corvallis, OR. As a Doctoral Student under the Rockwell International Doctoral Fellowship Program, University of Wisconsin, his research included experimental and theoretical investigations of polarization-altering guided wave optical devices. Since joining the Naval Research Laboratory, Washington, DC, he has been engaged in radar sea scatter research. Recent work includes the development of ultrawide-band, polarimetric systems for submerged mine studies, as well as the development of airborne radar systems for remote sensing of the coastal ocean.